This is a preprint, the final version is subject to change, of the American Mineralogist (MSA)
Cite as Authors (Year) Title. American Mineralogist, in press.
(DOI will not work until issue is live.) DOI: http://dx.doi.org/10.2138/am-2015-4961

Revision 1

In-situ oxygen isotope and trace element geothermometry of rutilated quartz from Alpine fissures

Danielle Ziva Shulaker[1], Axel K. Schmitt[2], Thomas Zack[3], and Ilya Bindeman[4]

[1]Department of Geological and Environmental Sciences, Stanford University, Stanford, CA 94305, U.S.A. E-mail: zivas@stanford.edu
[2]Department of Earth, Planetary, and Space Sciences, University of California Los Angeles, Los Angeles, CA 90095, U.S.A. E-mail: axel@oro.ess.ucla.edu
[3]Department of Earth Sciences, University of Gothenburg, Box 460, SE-405 30 Göteborg, Sweden. E-mail: thomas.zack@gu.se
[4]Department of Geological Sciences, University of Oregon, Eugene, OR 97403, USA. E-mail: bindeman@uoregon.edu

Abstract

Finely-acicular rutile intergrown with host quartz (rutilated quartz) is commonly found in hydrothermal veins, including the renown cleft mineral locations of the Swiss Alps. These Alpine cleft mineralizations formed between ~13.5 and 15.2 Ma (based on ages of rare hydrothermal monazite and titanite) at temperatures (T) of ~150-450°C (based on fluid inclusions and bulk quartz-mineral oxygen isotope exchange equilibria), and pressures (P) of 0.5-2.5 kbar (estimated from a geothermal gradient of 30°C/km). The potential of rutilated quartz as a thermochronometer, however, has not been harnessed previously. Here, we present the first results of age and T determinations for rutilated quartz from six locations in the Swiss Alps with vein country rocks that cover peak-metamorphic conditions between ~600 and <350°C. Samples were cut and mounted in epoxy discs to expose rutile (~30 to 1,400 μm in diameter) and its host quartz. Cathodoluminescence (CL) and back-scattered electron (BSE) imaging of host quartz and rutile inclusions, respectively, shows internal zonations which are nevertheless isotopically homogeneous. Newly developed Secondary Ionization Mass Spectrometry (SIMS) oxygen isotopic analyses protocols for rutile were combined with established analysis protocols for trace

elements (including Zr) and U-Pb ages in rutile, and Ti abundances in the host quartz. U-Pb rutile ages average 15.1±1.7 Ma (2σ), in excellent agreement with previous accessory mineral geochronometers. Pressure-independent T estimates, calibrated for low temperature conditions, from oxygen isotope fractionation between rutile and quartz in touching pairs are 310-576°C. Individual rutile needles vary in Zr abundances beyond analytical uncertainties, but average Zr-in-rutile inversely correlates with oxygen isotopic fractionation between quartz and rutile. Linear regression of the data yields:

$$T(^{\circ}\mathrm{C}) = \frac{26(\pm 9)}{0.07(\pm 0.01) - \mathrm{R}\ln x} - 273$$

with x = Zr ppm and R = 0.008314 (uncertainties scaled by the square root of the mean square of weighted deviates MSWD = 11; n = 9). This relationship supports previously recognized temperature-dependent Zr uptake in rutile, although widely used Zr-in-rutile thermometer calibrations based on high-T experiments are at variance with oxygen isotope exchange temperatures. By contrast, Ti-in-quartz lacks systematic relations with oxygen isotope temperatures. The discrepancy between low-T Ti-in-quartz thermometry on one side, and oxygen isotope and Zr-in-rutile thermometry on the other, suggests that Ti-in-quartz thermometry should be applied with caution for low-T (<500° C) rocks.

KEYWORDS

Rutilated quartz; Ti-in-quartz thermometer, Zr-in-rutile thermometer; Alpine fissures; Swiss Alps

INTRODUCTION

Rutile (TiO_2) is an accessory mineral most commonly associated with high-temperature (T) high-pressure (P) metamorphic rocks. Under these conditions, it can form as an accessory phase from the break-down of ilmenite (Luvizotto et al. 2009b) or biotite (Luvizotto and Zack 2009). Another mechanism for metamorphic rutile formation is exsolution from major phases such as quartz (e.g., Seifert et al. 2011) or garnet (e.g., Zhang et al. 2003). During low- and medium-grade metamorphism, rutile forms characteristic needle-like crystals, which is also common for low-pressure hydrothermal systems where rutile crystallizes within quartz veins (e.g., Ayers and Watson 1993; Deer et al. 1992), often intimately intergrown with quartz. Under conditions of high solubility, titanium (Ti)-rich minerals, like rutile, precipitate from a metasomatic aqueous fluid, and are later engulfed by quartz crystallization (Ayers and Watson 1993). Such conditions favoring rutile precipitation include tectonic unroofing – causing increased Ti solubility with decreasing pressure – or a decrease in H_2O activity by salt addition or dilution (Ayers and Watson 1993).

One prominent environment where hydrothermal rutile occurs are fissures or clefts that opened during tectonic stretching or bending of rocks. During late stage Alpine metamorphism, such cleft minerals precipitated from aqueous fluids that interacted with the host rock (Mullis et al. 1994; Mullis 1996; Sharp et al. 2005). Known as rutilated fissure quartz (aka sagenitic quartz, Venus' hair stone, fleches d'amour, or cupid's darts), this mineralization contains golden to reddish and brownish rutile needles which in some instances are crystallographically oriented within the host quartz, but in other cases are randomly orientated.

Rutilated quartz is of importance for several reasons: (1) equilibrium oxygen isotope fractionation between quartz and rutile is large, and has been well calibrated empirically and used as a thermometer (e.g., Matthews 1994; Agrinier 1991); (2) the temperature and pressure

dependence of zirconium (Zr) partitioning into rutile is a thermobarometer (e.g., Zack et al. 2004; Watson et al. 2006; Tomkins et al. 2007); (3) Ti solubility in the host quartz is also temperature- and pressure-dependent, and has been calibrated as a thermobarometer (e.g., Wark and Watson 2006; Thomas et al. 2010; Huang and Audétat 2012); and (4) rutile incorporates uranium and often little thorium and lead which enables it as a geochronometer (e.g., Mezger et al. 1989). Evidently, when coupled with host quartz, analysis of rutilated quartz has strong potential to improve geologic constraints for a gamut of crystallization conditions (temperature, pressure, and age) using a single sample.

This study presents the first results of age (t) and P-T determinations for rutilated quartz from six classical mineral locations in the Central Swiss Alps. Previous studies of Alpine cleft mineralization used rare hydrothermal monazite and titanite to constrain vein formation to ~13.5-15.2 Ma, postdating peak metamorphism by ~2.4 Ma (Janots et al. 2012; Sharp et al. 2005). However, the potential of rutilated quartz as a thermochronometer has not been harnessed previously. Because the Central Swiss Alps have been thoroughly studied for many years, it is an ideal place to develop the study of rutilated quartz as new technique for determining P-T-t parameters for late metamorphic hydrothermal activity in orogenic sites. The applicability of previously calibrated Zr-in-rutile and Ti-in-quartz thermometers can thus be determined for natural conditions of rutile and quartz precipitation at the low temperature spectrum (ca. 150->450°C; Sharp et al. 2005), beyond those achieved in experimental studies. Here it is of particular relevance that instead, quartz-rutile oxygen isotope exchange has been well calibrated at low temperature conditions (Agrinier 1991; Matthews 1994).

SAMPLE DESCRIPTIONS

Rutilated fissure quartz crystals were obtained from six locations within the Central Swiss Alps (Figure 1). In total, four general regions are represented: Samples 1, 2, and 6 are from locations along the southern border of the Gotthard Massif; Sample 3 is from a vein within the Pennine Bündnerschiefer unit; Sample 4 is from the Lepontine Dome comprising rocks of the Lucomagno-Leventina nappe, specifically the Leventina Gneiss; and Sample 5 was collected from folded non-metamorphic cover units within the Helvetic nappe (Frey et al. 1999). Rutile-bearing quartz crystals have well-developed crystal faces and samples from this study are approximately 2.5-4 cm in length. Quartz samples were cut into smaller fragments at optimal orientations to expose the rutile needles within the host quartz crystal at the mounting surface, which were then individually mounted into 2.54 cm diameter epoxy discs. Rutile and quartz standards (see below) were added to each sample mount, and placed as close as possible to the unknowns. Samples were imaged via electron imaging using a LEO 1430 VP scanning electron microscope (SEM) to assess size and rutile placement within the quartz, and to determine zoning patterns by BSE and CL imaging.

All rutile samples were confirmed to be rutile by Electron Backscatter Diffraction (EBSD). Only rutile exposed on the mounted sample fragment was analyzed. Per quartz crystal, the subset of rutile needles that were exposed and analyzed lack common orientations, except for Sample 2 where needles are sub-parallel. The size of the rutile needles in our samples (typically 10's to 100's of μm in diameter) exceeds those formed by exsolution from Ti-rich high-T quartz (Cherniak et al. 2007). Moreover, the absence of systematic orientation, and the occasional presence of euhedral adularia microcrystals decorating the rutile needles also argue against formation via exsolution (cf. Adachi et al. 2010), and instead imply co-crystallization of quartz and rutile from hydrothermal transport and leaching from host rock. Other impurities in the host

quartz (e.g., mica; ilmenite) were only investigated at reconnaissance levels using visual criteria and energy dispersive X-ray spectrometry energy dispersive spectrometer (EDS).

Sample 1

This sample of an Alpine rutilated fissure quartz crystal was collected at Alpe di Fieud, Gotthard Massif (46˚32'20.4"N; 8˚33'37.8"E; Figure 1, Figure 2). The turbid host quartz crystal contains two black-red rutile needles ~175 μm and 200 μm in diameter. The quartz appears to lack other mineral inclusions, though it is too dark to see inside. A fragment of this quartz crystal was mounted so that rutile needles are exposed near the outer portion of the quartz, in growth sectors which are light in cathodoluminescence (CL) images (Figure 2a). The exposed rutiles intersect the cut surface nearly perpendicular to the c-axis of the rutile.

Sample 2

Sample 2 was collected from quartz veins in Bündnerschiefer at Turbechepf, Feldbach, Binntal (46˚24'4.6"N; 8˚15'51.8"E; Figure 1) in the Gotthard Massif. The quartz crystal is translucent and contains many impurities. There are numerous internal fracture planes throughout the quartz, some of which are composed of scattered black, platy mineral inclusions. These inclusions were not exposed on the mounted fragment and therefore not analyzed, but tentatively identified as biotite, as Bündnerschiefer is largely composed of metamorphosed phyllites and schists, which are rich in micas (Sharp et al. 2005). Some rutile needles have been fractured via fracture planes, which appear as microscopic strike-slip faults within the quartz. The quartz CL image is dark and lacks visible zonation. Areas of orange coloration on the quartz exterior are possibly due to iron oxidation or micro-rutile growth. Rutile crystals physically encapsulated within the quartz crystal are divided into two populations: thin, golden hair-like needles that expand the length of the quartz, and needles similar to Sample 1 which are more

stubby and dark in color. Of the exposed rutiles on the mount surface, those analyzed in this study are oriented in the same direction. However, there are several rutiles that are exposed but not analyzed due to their small size. In addition to rutile, ilmenite is present as hair-like needles, which are thinner in diameter than the rutiles. Rutiles range from 10 to 45 μm in diameter; however some larger rutiles ~100 μm in diameter that were present in the quartz were not analyzed because the grains were "plucked out" during mount preparation and polishing.

Sample 3

The third quartz sample was collected at Pi Aul, Vals (46˚37'4.9"N; 9˚7'44.2"E; Figure 1) in the southern Gotthard Massif. The quartz crystal is very translucent and contains few annealed fracture planes. CL images show a thin, light growth layer on the outside and larger, darker growth zones towards the center of the quartz. Rutiles are either golden or black hair-like, expanding over the length of the quartz. Rutiles exposed on the surface that were analyzed are oriented in the same direction and were intersected at an acute angle relative to their c-axis. Only one sizable (~200 μm in diameter) rutile crystal was analyzed.

Sample 4

Sample 4 was collected from a vein in orthogneiss host rock at Vaido, Leventina (46˚29'2.3"N; 8˚47'43.2"E; Figure 1), which is part of the Lucomagno-Leventina Nappe (Rütti et al. 2005; Rütti 2003; Milnes 1978; Geological Institute, University of Bern, and Federal Office for Water und Geology 2005). The quartz crystal is opaque with few brown impurities and small fluid inclusions along fracture planes. There are only two sizable golden hair-like rutile needles with microscopic adularia attached which are sectioned to expose areas ~100 μm and 150 μm in diameter. The host quartz shows distinctive growth sector zoning in CL imaging (Figure 3). The

smaller rutile needle is within the light zone and the larger needle is within the dark zone of the quartz. Both rutiles are aligned and intersected in approximately the same orientation.

Sample 5

The fifth sample was collected at Elm, Steinbach (approximate location: 46°54'N; 9°8'E; Figure 1) within the Helvetic Zone. The fissure quartz crystal is turbid and contains only one large dark brown-black rutile ~1000 μm in diameter. The rutile is exposed on the mount surface in a rectangular shape as it is sectioned at a slightly acute angle relative to its c-axis.

Sample 6

Sample 6 was collected as a lose crystal in the Bündnerschiefer in Binntal, Binn (approximate location: 46°21'N; 8°12'E; Figure 1). The euhedral quartz crystal is translucent with few internal cracks, small, localized areas of orange coloration, and <1 mm sized pieces of schistose host rock adherent to a crystal face. Many of the internal fracture planes are aligned along an angle inclined from the c-axis of the quartz. Some large fracture planes are almost perpendicular to the c-axis and contain few fluid inclusions. Along the fracture plane is a dark green-brown coloration thought to result from mica inclusions (as per Sample 3 observations). These inclusions were not exposed in the mounted sample, and therefore not analyzed. CL intensity across the sectioned quartz interface is largely uniform (Figure 4a). The quartz contains one smaller rutile (~200 μm in diameter; Figure 4b) which is dark brown-red in hue, and a larger rutile (~1400 μm in diameter; Figure 4c) of a spectacular red-brown color. Both needles intersect the mount surface at an inclined angle from their c-axis. Adularia is attached to the needles. They show zoning in back-scattered electron (BSE) imaging with most of the outer regions of the crystals being BSE dark (Figure 4b-4c).

SAMPLE PREPARATION AND ANALYTICAL METHODS

Seven natural and synthetic rutiles previously described in Luvizotto et al. (2009a) and Schmitt and Zack (2012) were selected as potential standards. Several gram of each were crushed into small fragments of which the larger (ca 1.5 mg each) were randomly selected for CO_2-laser fluorination analysis and the smaller (ca 100-200 μm) for SIMS analysis.

Please refer to above section for sample preparation and mounting methods. Prior to Secondary Ionization Mass Spectrometry (SIMS) and laser ablation inductively-coupled plasma mass spectrometry (LA-ICP-MS) analysis, all samples were imaged via electron imaging using a LEO 1430 VP scanning electron microscope (SEM) and imaged in BSE and CL. All samples were gold (Au) coated for SIMS analysis; this conductive Au coating was removed by gentle re-polishing prior to LA-ICP-MS analysis.

SIMS Analysis

Isotopic and trace element analyses (^{18}O-isotopes, Ti-in-quartz, and U-Pb) were carried out by SIMS at UCLA using the CAMECA ims1270. Figures 2-4 show the relative placement of analytical spots via SIMS analyses.

Oxygen Isotopes.

Because procedures for SIMS oxygen isotope analysis of rutile have not been published in detail, we report oxygen isotope data for newly developed rutile standards, independently analyzed by laser fluorination (Table 1; Figure 5), and summarize experimental results that were conducted to assess the accuracy and precision of this technique. The fragments from natural and synthetic rutiles were analyzed in replicate (n = 2-4; except for rutile Diss for which very limited material was available; Table 1) by CO_2-laser fluorination in the University of Oregon stable isotope lab following techniques outlined in Bindeman (2008). A NewWave 35 W laser heated

the samples in the presence of purified BrF_5 reagent to liberate oxygen. Oxygen gas generated in the laser chamber was then purified cryogenically, and by using a mercury vapor diffusion pump. The purified oxygen gas was subsequently converted to CO_2 gas using small platinum-graphite converter. CO_2 gas was analyzed on a MAT 253 mass spectrometer in a dual inlet mode. Four garnet standards (GMG-2 $\delta^{18}O$ = 5.75 ‰ and UOG $\delta^{18}O$ = 6.52 ‰) were analyzed interspersed with the unknowns, and used for correction of isotopic fractionation. Uncertainties for the unknowns are estimated from the reproducibility of the standards which is <0.1 ‰ (1 standard deviation; s.d.) during the course of an analytical session. Replicates of R10B and R13 reproduced well within analytical uncertainty, making both samples suitable standards for in-situ oxygen isotope analysis. On the other hand, minor variability in excess of the analytical error exists for 210 and 202 (and possibly for Sy, Diss, and 213; Table 1).

Small fragments from the same rutiles were placed in random orientation on adhesive tape, and cast in epoxy using a 2.54 cm diameter plastic ring mold. The epoxy mount was then ground using SiC paper and 1-3 μm diamond film to create a flat surface. Rutile standard R10b ($\delta^{18}O$ = 6.60‰; Table 1) was used as the primary standard because it is widely used as a geochronology standard (Luvizotto et al. 2009a; Schmitt and Zack, 2012), and it shows excellent reproducibility in replicate laser fluorination analyses indicating homogeneity for mg-sample sizes. For SIMS oxygen isotope analysis, however, the reproducibility of R10b (and in fact all other rutiles tested) showed significantly more spread than that of borosilicate glass analyzed under the same conditions (Figure 6). We attribute this to a crystal-orientation bias of the instrumental mass fractionation (IMF), which is also present in ion beam analysis of Pb/U (Schmitt and Zack 2012; Taylor et al. 2012). To assess the precision and accuracy achievable in SIMS rutile analyses, we analyzed all rutile standards listed in Table 1 in several round-robin

sessions using R10b as the primary standard to correct for IMF. Three analytical and correction protocols were tested: (1) Cs^+ primary beam accelerated at 10 kV and a beam current of ~6 nA focused by a 100 μm aperture in the L4 position of the ims1270 primary column to a spot ~20 μm in diameter; the IMF correction is based on the average of the primary standard during the analytical session (Trail et al. 2009); (2) the same analytical conditions as in (1), but using an IMF correction based on a linear fit of R10b IMF vs. $^{16}O^-$ intensity normalized to the Cs^+ intensity ("yield correction"); and (3) Cs^+ primary beam accelerated at 5 kV with an intensity of ~2 nA, and a spot diameter of ~25 μm, rationalizing that a lower impact energy will mitigate bias caused by variations in crystal orientation (Kita et al. 2011; Schmitt and Zack 2012). All protocols used a normal-incidence electron gun for charge compensation, and secondary ions were detected simultaneously in two Faraday cups (FC) in multi-collection for 120 sec following a 30 sec pre-sputtering period during which FC backgrounds were recorded. Results for the different protocols are compared in Table 1 and Figure 6. Protocol (3) yields the lowest average standard deviation for rutile, as well as the least deviation from the laser fluorination value. A disadvantage of a 5 kV Cs^+ beam, however, is that the reproducibility of analyses of the borosilicate glass deteriorated to ~0.3-0.5 ‰ (1 s.d.), whereas it was ~0.1-0.2 ‰ (1 s.d.) for the 10 kV Cs^+ beam. Procedure (2) provides a slight improvement over (1) for rutile; no effect was noted for the glass. Based on these experiments, we conclude that for analyzing only rutile, procedure (3) appears preferable because it mitigates crystal-orientation dependent IMF. Procedures that correct IMF based on independently established crystal orientation (e.g., by applying EBSD) await future testing. For the analysis of $^{18}O/^{16}O$ in unknown rutile needles and host quartz, we selected procedure (2) as a compromise that would allow us to analyze rutile and quartz under the same analytical conditions, while maintaining high precision for quartz analysis.

Late Bishop Tuff quartz ($\delta^{18}O$ = 8.21 ‰; Bindeman and Valley 2002) and R10b rutile ($\delta^{18}O$ = 6.60 ‰; this study) were used for IMF correction of unknown quartz and rutile, respectively. Spots in the host quartz were placed on areas directly encompassing the rutile needle (Figures 2-4). Rutile crystals exposed on mount surfaces were analyzed for all samples if their diameter was larger than the Cs^+ beam diameter. Most rutile needles accommodated 1-2 spot analyses, or more if larger. Because quartz from Sample 4 had the most visible growth sector zoning in CL, it was selected for an oxygen isotope traverse over different growth sectors (light or dark regions of the CL image) of the host quartz. For thermometry, we calculated the isotopic difference between quartz and rutile $\Delta^{18}O_{qtz\text{-}rut} = \delta^{18}O_{qtz} - \delta^{18}O_{rut}$. $\approx 1000\ \ln\alpha_{qtz\text{-}rut}$ using an coefficient A = 5.02 (Matthews 1994) in the equation $1000\ \ln\alpha = A \times 10^6\ T^{-2}$. For the SIMS protocol (2) applied here, the total uncertainty for $\Delta^{18}O_{qtz\text{-}rut}$ is estimated to be ~1 ‰ (2σ) based on propagating the average reproducibility of R10b rutile and Late Bishop Tuff quartz (standard deviations of 0.48 ‰ and 0.15 ‰, respectively).

Ti-in-quartz.

The original titanium-in-quartz geothermometer, "TitaniQ," was based on the experimental calibration of Ti abundances in quartz which were analyzed by electron microprobe (EMPA) and SIMS (Wark and Watson 2006). Subsequent calibrations aimed to better accommodate temperature and pressure effects on Ti solubility in quartz (e.g. Thomas et al. 2010). To assure optimal intercomparison between the calibration and our samples, we obtained synthetic quartz from the Thomas et al. (2010) calibration with the following Ti abundances: QTIP39 = 813 ppm, QTIP38 = 380 ppm, QTIP14 = 100 ppm, and QTIP7 = 18 ppm. SIMS analysis on the ims1270 was performed in multi-collection analyzing $^{48}TiO^-$ and $^{30}SiO_2^-$ in two electron multipliers (EM) using techniques described in Harrison and Schmitt (2007). The

advantage of this technique is higher internal precision through multi-collection, and the faster sputter rate of the Cs^+. This aids in removing surface contamination which was achieved by pre-sputtering the target area for 10 minutes with a 30 μm raster at 0.5 nA. Following the pre-sputter interval, the Cs^+ primary beam was focused to a 10 μm spot in the center of the pre-sputtered area. A normal incidence electron gun was used for charge compensation. Secondary ion intensities were integrated for 120 seconds, and a stable $^{48}TiO^-$ intensity was observed during the run, indicating that any surface contamination was successfully removed despite the host quartz being measured adjacent to rutile. A linear working curve was established using QTIP38, QTIP14, and QTIP7. QTIP39 yielded apparent Ti abundances that were ~13 % too low; this was attributed to heterogeneity of QTIP39 which was also described in Behr et al. (2011). TitaniQ crystallization temperatures were then calculated at geologically reasonable pressures (see below) using calibrations from Thomas et al. (2010) and Huang and Audétat (2012).

U-Pb.

The same rutile needles analyzed for oxygen isotope composition were also targeted for U-Pb dating. An O_2^+ primary beam at ~110-190 nA focused to a ~25 μm diameter spot was used as described in Schmitt and Zack (2012). The duoplasmatron extraction potential was +15.5 kV and the sample potential was set to +4.5 kV. Secondary ion intensities were collected using a single (axial) EM in peak-switching mode. Pb/U relative sensitivity factors (RSF) were calibrated on standard rutile R10b (1099 Ma; Luvizotto et al. 2009) by linear regression against measured UO_2^+/U^+. Data are plotted uncorrected for common Pb in a Tera-Wasserburg Concordia diagram, and the age is calculated from the Concordia intercept of a linear regression (Figure 7). U and Th concentrations were estimated from $UO_2^+/Ti_3O_4^+$ and ThO_2^+/UO_2^+ in

comparison to rutile standard R10b (50 ppm U; Luvizotto et al. 2009a). A ThO_2^+/UO_2^+ RSF of unity was assumed, given the extremely low Th in standards and unknowns.

LA-ICP-MS Analysis

Zr-in-rutile.

Zr-in-rutile analysis was carried out by the LA-ICP-MS system (213 nm NWR New Wave laser coupled to an Agilent 7500a) at the University of Gothenburg, Sweden. High sensitivity (ca 50 cps ^{90}Zr per ppm Zr at 10 μm spot size) was ensured by operating a second rotary pump for the vacuum between skimmer and sample cone, and by adding 5 ml N_2/min to the carrier gas. Trace element analysis of rutile are routinely analyzed with 10 micron spot sizes, a laser fluence of ca 7 J/cm^2 at 10 Hz. A large sample chamber allows all samples (except Sample 5, which was investigated in an extra run) and standards to be analyzed in one run. Standardization of rutile by using the NIST SRM 610 glass (using compilation of Jochum and Stoll 2008) as a primary standard is found to be sufficient. Accuracy is evaluated by measuring two R10 and one R10b fragments at different positions in the sample chamber: Zr concentrations are 868 ppm, 872 and 826 ppm, respectively; systematically higher but within 10% of the 789 ppm reported in Luvizotto et al. (2009). Zr concentrations of other standards are also always within better than 10% of published values: 227 ppm for TNT150 titanite glass (225 ppm; Klemme et al. 2008), 41.2 ppm for GSD-1G glass (42 ppm; compilation in Jochum and Stoll 2008) and 181 ppm for BCR-2G glass (184 ppm; compilation in Jochum and Stoll 2008). Further details on the instrumental setup at the University of Gothenburg can be found in Cornell et al. (2013); details on rutile trace element analysis in Zack et al. (2011).

RESULTS

Age of Alpine rutilated quartz

We report a total of 21 U-Pb spot analyses for eleven different rutile needles from all six fissure quartz samples (see Appendix 1 for complete list of results). Of the rutile needles with sufficient uranium for dating, U and Th concentrations vary from 0.025 to 14.7 ppm and 10 to 13400 ppb, respectively. Most rutile needles have abundances of 2-7 ppm U, with the highest abundances in Samples 2 and 4. Sample 5 had the lowest U concentrations (<1 ppm). Samples 1 and 6 with the highest T estimates (see below) also display the highest radiogenic yields, and thus the lowest age uncertainties. Because radiogenic Pb concentrations were typically low, U-Pb data were plotted uncorrected on a Tera-Wasserburg diagram (Figure 7). Calculating common-Pb corrected ages for samples 1 and 6 using values for common Pb from regional galena (Graeser 1968; Hofmann and Knill 1996) as an anchor for the regression line yields overlapping ages of 15.1±2.1 Ma (MSWD = 2.0; n = 4; anchored common $^{207}Pb/^{206}Pb = 0.836\pm0.001$) and 15.7±1.3 Ma (MSWD = 1.8; n = 5; anchored common $^{207}Pb/^{206}Pb = 0.846\pm0.003$), respectively. For the other samples, the ages are too imprecise to be meaningful due to low radiogenic Pb, but linear regression through all data yields a common $^{207}Pb/^{206}Pb = 0.833\pm0.006$ consistent with those of galena mineralization hosted by regional rocks (from 0.836 to 0.853; Graeser 1968; Hofmann and Knill 1996), justifying the approach of anchoring the rutile regressions to a common Pb value corresponding to regional galena. A Concordia intercept age of 15.1±1.7 Ma (mean square of weighted deviates MSWD = 2.1; n = 21) is obtained for all data with a slightly elevated MSWD which is likely due to different common Pb compositions, and/or minor age differences between the samples.

Rutilated quartz thermometry

Within each mount, 1- 2 rutile needles and adjacent quartz were analyzed with replicate spots on rutile and quartz where possible, and results are reported as the average values for each area per sample (see Appendix 2 for oxygen isotope and Ti-in-quartz data). Because most replicate analyses were within analytical uncertainties, data is reported as average values per rutile needle and adjacent host quartz (Table 2). Average oxygen isotope values in a traverse on Sample 4 reveal no significant contrast between light and dark CL domains (Figure 3). Similarly, $\Delta^{18}O_{qtz\text{-}rut}$ in individual samples typically overlaps within 2σ (Table 2). Heterogeneities exceeding the ±10% relative analytical uncertainties estimated from replicate standard analyses were observed for Zr-in-rutile (e.g., Figure 4). In the absence of any criteria that would permit us to disregard high or low Zr values, we use averages and standard deviations for Zr-in-rutile (Table 2), recognizing that the unknowns are compositionally heterogeneous (see Appendix 3 for Zr-in-rutile and trace element laser data).

Crystallization temperatures were obtained from calibrations for oxygen isotope fractionation between quartz and rutile (Matthews 1994), Ti-in-quartz solubility (Thomas et al. 2010; Huang and Audétat 2012), and Zr-in-rutile solubility (Zack et al. 2004; Tomkins et al. 2007). We use the empirical Matthews (1994) calibration for the temperature-dependence of quartz-rutile oxygen isotope fractionation, acknowledging that other experimental calibrations (e.g., Chacko et al. 1996) yield essentially indistinguishable results, while increment methods are divergent (Zheng 1991). For pressure-dependent Zr-in-rutile and Ti-in-quartz, we assumed a pressure of 2 kbar for Alpine fissure formation based on geological constraints (Figure 8), but explored a wide pressure range from 0 to 8 kbar to assess the potential impact of pressure uncertainty on the thermometers (Figure 9).

Taken at face value (Figure 9), Ti-in-quartz thermometry would indicate a narrower T window (between ~480 and 380°C) for rutilated quartz formation than the oxygen isotope fractionation and Zr-in-rutile thermometer (using Zack et al. 2004, adjusted for P) which yield T between ~570 and 320°C (please see Appendix 4 for complete list of data plotted in Figure 9). A linear regression of lnZr vs. 1/T (using the Matthews 1994, quartz-rutile oxygen isotopic fractionation) yields the following fit (mean square of weighted deviates MSWD = 11; n = 9):

Eq. 1 $$T(^{\circ}\mathrm{C}) = \frac{26(\pm 9)}{0.07(\pm 0.01) - \mathrm{R}\ln x} - 273$$

with x = Zr-in-rutile in ppm and R = 0.008314 (total 2σ uncertainties in parentheses). The high MSWD indicates excess scatter, possibly due to Zr-in-rutile heterogeneity and potentially differences in pressure of vein formation for the different sample locations. Regardless of the causes of scatter, it is propagated into the stated uncertainties by multiplying the regression slope and intercept errors with the square-root of the MSWD. Notably, this slope is significantly different from the experimental calibration by Tomkins et al. (2007) extrapolated to low T. The slope is, however, similar to that of the empirical calibration in Zack et al. (2004), although the observed Zr abundances in rutile are above those predicted by Zack et al. (2004). This could be due to a pressure effect (decreasing Zr solubility at higher pressure; Tomkins et al. 2007) because the empirical model of Zack et al. (2004) is based on high-P metamorphic rocks.

Ti-in-quartz measured in the host adjacent to the rutile needles by contrast lacks systematic relationships between lnTi and 1/T (Figure 9). Qualitatively we find the highest Ti-in-quartz for the highest quartz-rutile oxygen isotope temperatures, but at T <500°C Ti-in-quartz appears to be quasi-invariant of the quartz-rutile oxygen isotope temperatures. The Ti-in-quartz temperature of Huang and Audétat (2012) are broadly consistent with the quartz-rutile oxygen isotope temperatures near 400°C, but significantly lower than those predicted by Thomas et al.

(2010). Because our Ti-in-quartz values often fall below the predicted values (except for Sample 5), we can rule out that our analyses are affected by Ti contamination from adjacent rutile.

DISCUSSION

Age of Alpine fissure mineralization

The $^{206}Pb/^{238}U$ Concordia intercept ages (Figure 7) for two rutilated quartz samples of 15.1 and 15.7 Ma are in excellent agreement with previous determined ages for Alpine cleft formation, postdating peak metamorphism during rapid cooling 20-16 Ma (Sharp et al. 2005, and references therein). Mullis (1996) used exhumation rates and trapping temperatures of fluid inclusions to estimate the timing of fissure quartz crystallization. According to this model, retrograde quartz crystallization occurred in three stages from 20 to 15 Ma. Zircon fissure-track ages reflect two tectonic exhumation events accompanying faulting at ca. 18-15 Ma and 15 Ma to present (Bernet et al. 2001). Published zircon fissure-track ages and K/Ar and Rb/Sr cooling ages of fissure and host-rock muscovite and biotite overlap with the dated Alpine vein growth stages at ~15 Ma (Mullis et al. 1994, and references therein). Previous studies of veins in the same locations as our study yielded equivalent ages, e.g. by dating hydrothermal titanite crystallization at 15.0±0.04 Ma using thermal ionization mass spectrometry (TIMS; Sharp et al., 2005). Rare large (mm-sized) hydrothermal monazite from Alpine veins yielded SIMS $^{208}Pb/^{232}Th$ ages between 15.2±0.3 Ma and 13.5±0.4 Ma, whereas initial ^{230}Th excess shifted $^{206}Pb/^{238}U$ to apparent older ages (Janots et al. 2012). Because Th/U is characteristically low in rutile, initial U-series disequilibrium was likely minor although the effects of ^{234}U disequilibrium in hydrothermal fluids are unknown. Regardless of this uncertainty, the close overlap between

$^{206}Pb/^{238}U$ ages for rutile and those of titanite and monazite are in support of vein-formation and fissure quartz precipitation during initial tectonic unroofing of the Alps at ~15 Ma.

Geological context

Samples 1-6 fall into four broad Alpine geotectonic units (Figure 1). Samples 1, 2, and 6 are within the southern border of the Gotthard Massif, on the northern border of the Lepontine Dome. Temperature-pressure estimates for cleft formation in this region range from 400-450˚C at 2.4-3.8 kbar (Mullis et al. 1994). Mullis (1996) also determined temperatures of fluid populations in quartz crystals from southern Gotthard massif to be 420˚C (older fluid population) and 240˚C (younger). Poty et al. (1974) analyzed fluid inclusions in quartz crystals from three locations in close proximity to Samples 1, 2, and 6, which resulted in PT estimates of 380-505˚C and 1.4-2.7 kbar. Sample 3 (Vals) is from Bündnerschiefer in the Pennine zone for which earlier temperature estimates for post-peak metamorphism are >350˚C (Ring 1992). Correlating a temperature of ~350˚C with retrograde P-T path of the Vals region yielded a minimum pressure of ~2.5 kbar (Ring 1992). Sample 4 is from Faido, which lies in the Lucomagno-Leventina nappe. Myrmekite presence and phengite barometry yield PT constraints of ~550-600˚C and 2-8 kbar (Rütti 2003). Sample 5 is from a vein within Helvetic nappe rocks which comprises folded, non-metamorphic cover units of late Carboniferous-Cretaceous or Eocene age (Frey et al. 1999). Metamorphic T for this part of the Helvetic nappe are <350 ˚C (Bousquet et al. 2012).

These general P-T constraints are only broadly comparable to our data because literature study locations and rutilated quartz sampling locations from this study are spatially uncorrelated. Moreover, literature samples may pre-date (in the case of metamorphic geothermobarometry) or post-date (in the case of secondary fluid inclusions) vein mineralization, and therefore over- or underestimate vein formation temperatures, respectively. Nevertheless, it is clear from these

geological constraints that temperature estimates between ~500 and 300°C obtained from various geothermometers applied to rutilated quartz are geologically reasonable: they are either equivalent (Sample 6) or fall below estimated peak metamorphic temperatures, consistent with retrograde vein formation (Samples 1-5). Moreover, there is a broad correlation between the lowest T estimates from rutilated quartz and peak metamorphic T (from high to low: samples 4, 2, 3, and 5) which suggests that metamorphic paleotemperature gradients persisted to the time of vein formation. Similar considerations hold for bulk oxygen isotope exchange thermometry data between ~450 and 150°C for Alpine quartz veins (Sharp et al. 2005). Sharp et al. (2005) also demonstrated that $\delta^{18}O$ values of quartz veins are indicators of the host rock-type, and that fluids were in equilibrium with the rock. Their $\delta^{18}O$ values for vein quartz crystals from different host rocks range between ~10 and ~28 ‰; this is exactly the range we find for the host quartz of our rutilated quartz samples. We therefore conclude that thermometry constraints from rutilated quartz are fully supported by existing geological data. A detailed comparison between the different thermometers, however, reveals that intercalibration uncertainties are substantial, and that such discrepancies remain a significant impediment to accurate low-T geothermobarometry.

Geothermometer intercalibration

The in-situ analysis techniques (SIMS, LA-ICP-MS) employed here enable spatially co-registered determination of oxygen isotopic compositions and trace element abundances in small rutile inclusions and its host quartz. Although some rutilated quartz contains mm-sized rutile, acicular rutile in quartz is more typically ~20-50 μm in cross section which requires high spatial resolution techniques to avoid mixing between host and inclusion. Even for larger crystals, the small spot sizes of SIMS and LA-ICP-MS is advantageous because it permits an assessment of zoning in rutile or its quartz host.

Zr-in-rutile.

Early Zr-in-rutile thermometers (Zack et al. 2004; Ferry and Watson 2007) did not specifically calibrate for pressure, and therefore the thermometry equation used in this study is that of Tomkins et al. (2007) which specifically accounts for pressure effects accompanying temperature dependence of Zr-in-rutile. Zr-in-rutile thermometry using the experimental calibration of Tomkins et al. (2007) consistently yields temperatures higher than oxygen isotope fractionation temperatures using the Matthews (1994) calibration. Unless geologically unreasonably high P is invoked (exceeding the brittle crustal realm in which the fissures formed), a significant discrepancy between most predicted and observed Zr-in-rutile temperatures remains (Figure 9).

Systematic bias could result from one or a combination of several factors: analytical bias (energy dispersive X-ray spectrometry EDS in Tomkins et al. 2007, vs. LA-ICP-MS applied here), rutile heterogeneity (e.g., caused by inclusions or contamination), bias in calibration or analysis of the quartz-rutile oxygen isotope thermometer, violation of the equilibrium with zircon (or - less likely - quartz), or misfits in the extrapolation of high-T experiments to low-T conditions. We cannot comment on the EDS analytical conditions because Tomkins et al. (2007) present no data that would verify the accuracy of their analytical approach. Rutile heterogeneity is clearly an issue because we have encountered heterogeneity between spots and even within individual ablations (e.g., Figure 4). These are beyond analytical uncertainties, and may account to a large extent for the scatter observed in the data. Nevertheless, the overall consistency between oxygen isotopic fractionation and Zr-in-rutile suggests that these intra-sample heterogeneities are averaged out by replicate analyses. In the absence of other studies on oxygen isotopic fractionation between quartz and rutile, the possibility of bias in the Matthews (1994)

calibration cannot be completely ruled out. We note, however, that quartz-rutile fractionation data in Matthews (1994) are consistent with those from natural samples and hydrothermal experiments (Agrinier 1991; Matthews and Schliestedt 1984, Chacko et al. 1996), with calibration differences generally less than the analytical uncertainties reported here. Moreover, rutile and quartz have high relative closure temperatures for isotopic resetting (Moore et al. 1998; Chacko et al. 1996; Giletti and Yund 1984), and the absence of isotopic zonation in rim-core profiles across quartz crystals implies that post-crystallization isotopic exchange is insignificant. SIMS artifacts due to crystal-orientation bias for oxygen isotope analysis of rutile are encompassed by our conservative uncertainty estimates (corresponding to an approximately ±50°C 2σ temperature error at 500°C); unrecognized bias can be dismissed because of the systematic trend between lnZr and quartz-rutile oxygen isotopic fractionation.

Second to last, we consider the requirement of rutile crystallizing in the presence of zircon and quartz, for if zircon has no communication with rutile when it forms, rutile will contain less Zr and therefore show a lower temperature estimate (Zack et al. 2004). We have no direct evidence for the presence of zircon at our sampling locations, but for one of our study areas (Binntal) hydrothermal zircon has been reported (Praeger and Crumbach 2004). Moreover, zircon is an omnipresent accessory mineral in Alpine fissure country rocks, and from the complete equilibration between precipitating fluid and host rock (Sharp et al. 2005), we infer equilibration between aqueous fluid and zircon.

A last remaining possibility for bias between Zr-in-rutile and oxygen isotopic thermometry is the problem of extrapolating high-T Zr solubility experiments to low T. Tomkins et al. (2007) recognized that Zr-in-rutile at high-T can exceed Henry's Law limits: their experimental rutile crystallized at T of up to 1500°C contained up to 17 wt% ZrO_2. A constant

interaction energy term was introduced by Tomkins et al. (2007), but without independent constraints it is difficult to assess if this correction is adequate, weakening reliable extrapolation to low Zr abundances characteristic for low-T rutile. Interestingly, the empirical calibration by Zack et al. (2004) who used low-T assemblages which at their lower end overlap with temperatures obtained for our rutilated quartz samples, shows a very similar slope than the fit in equation 1. Samples from Zack et al. (2004) have crystallization pressures of 16 – 18 kbar, an order of magnitude higher than our samples, which may account for higher-than-predicted Zr-in-rutile for low-P Alpine fissure rutilated quartz compared to the Zack et al. (2004) model. Clearly, better calibrations for Zr-in-rutile are needed to fully understand the pressure and compositional dependence of Zr partitioning in rutile at low T. We argue that with refined constraints on the pressure-independent oxygen isotopic fractionation between rutile and quartz, this may be achieved through the study of natural rutilated quartz.

Ti-in-quartz.

Ti-in-quartz temperatures were calculated using equations found in Thomas et al. (2010) and Huang and Audétat (2012). Temperatures calculated from Thomas et al. (2010) yield temperatures that are consistently lower than those calculated by oxygen isotope fractionation or Zr-in-rutile. Conversely, calculated Ti-in-quartz temperatures from Huang and Audétat (2012) yield values that are broadly similar to other thermometry techniques.

The original TitaniQ equation was experimentally determined at pressures from 5 to 20 kbar at 700-940˚C (Thomas et al. 2010). Huang and Audétat (2012) recalibrated TitaniQ at P-T conditions of 1 - 10 kbar and 600 – 800°C taking care to minimize kinetic effects which lead higher Ti incorporation in quartz. This might explain why the Huang and Audétat (2012) calibration generally yields closer agreement to the other thermometers applied here. A general

concern is that experimental samples used for calibrations have Ti-in-quartz concentrations that are several orders of magnitude greater than for the hydrothermal quartz analyzed here. Extrapolating experimental results to significantly lower temperatures by several hundred degrees could result in incongruity between natural and experimental samples. Regardless of this fundamental problem of experimental calibration at vastly different trace element abundances, the lack of correlation between Ti-in-quartz and the other thermometric indicators investigated here (oxygen isotopic exchange and Zr-in-rutile) is disconcerting regarding the applicability of Ti-in-quartz thermometry at low (<500° C) temperatures.

IMPLICATIONS

Rutile contains useful geochemical information that can be used to discover condition and timing of events, as it is a common accessory mineral as well as a common hydrothermal mineral. The role of rutile as a thermochronometer can be expanded to many geological settings, from subduction to orogeny to constraining timing and conditions of post-metamorphic hydrothermal fluid flow and mineralization.

Alpine rutilated fissure quartz formed after peak metamorphism 15.1±1.7 Ma during Alpine unroofing. The rutile crystallization age from this study matches previous Alpine cleft mineralization studies that dated accessory monazite and titanite. Temperature and pressure estimates record vein crystallization conditions in various locations throughout the Central Swiss Alps, which also agree with numerous previous studies of the area.

The presence of rutile in quartz in clefts from the Alps over a wide temperature range can help to determine the applicability of Ti-in-quartz and Zr-in-rutile thermometers to conditions below experimental calibrations because quartz-rutile oxygen isotope exchange has been well

calibrated close to natural temperature conditions for rutilated quartz. Because of discrepancies between thermometers, it is clear that more research and thermodynamic modeling is needed in order to better understand how P and T affects Zr incorporation in rutile. The Ti-in-quartz thermometer, by contrast, appears to be compromised by non-systematic Ti partitioning in low-grade metamorphic or hydrothermal environments. Rutilated quartz thus shows itself to be a promising thermochronometer because of its ability to be analyzed reliably using a variety of different techniques which can be evaluated for temperature concordance.

ACKNOWLEDGMENTS

Katie Kumamoto is thanked for EBSD work; Remo Zanelli for providing the samples; and Arfved Brandberg for his continual support and guidance throughout the course of this project. We greatly appreciate constructive reviews by Andreas Audétat, an anonymous reviewer, and Associate Editor Fidel Costa. Support was provided by grant EAR -844772, Za285/6-2 and Za285/7-1. The ion microprobe facility at UCLA is partly supported by a grant from the Instrumentation and Facilities Program, Division of Earth Sciences, National Science Foundation.

REFERENCES CITED

Adachi, T., Hokada, T., Osanai, Y., Toyoshima, T., Baba, S., and Nakano, N. (2010) Titanium behavior in quartz during retrograde hydration: Occurrence of rutile exsolution and implications for metamorphic processes in the Sør Rondane Mountains, East Antarctica. Polar Science, 2, 222-234.

Agrinier, P. (1991) The natural calibration of $^{18}O/^{16}O$ geothermometers: application to the

quartz-rutile mineral pair. Chemical Geology, 91, 49-64.

Ayers, J.C., and Watson, E.B. (1993) Rutile solubility and mobility in supercritical aqueous fluids. Contributions to Mineralogy and Petrology, 114, 321-330.

Behr, W.M., Thomas, J.B., and Hervig, R.L. (2011) Calibrating Ti concentrations in quartz for SIMS determinations using NIST silicate glasses and application to the TitaniQ geothermobarometer. American Mineralogist, 96, 1100–1106.

Bernet, M., Zattin, M., Garver, J.I., Brandon, M.T., and Vance, J.A. (2001) Steady-state exhumation of the European Alps. Geology, 29, 35-38.

Bindeman, I.N. (2008) Oxygen isotopes in mantle and crustal magmas as revealed by single crystal analysis. Reviews in Mineralogy and Geochemistry, 69, 445-478.

Bindeman, I.N., and Valley, J.W. (2002) Oxygen isotope study of the Long Valley magma system, California: isotope thermometry and convection in large silicic magma bodies. Contributions to Mineralogy and Petrology, 144, 185-205.

Bousquet, R., Oberhaulmnsli, R., Schmid, S.M., Berger, A., Wiederkehr, M., Robert, C., Möller, A., Rosenberg, C., Zeilinger G., Molli, G., and Koller, F. (2012) 1:1000000. Metamorphic Framework of the Alps. Commission for the Geologic Map of the World.

Chacko, T., Hu, X., Mayeda, T.K., Clayton, R.N., and Goldsmith, J.R. (1996) Oxygen isotope fractionations in muscovite, phlogopite, and rutile. Geochimica et Cosmochimica Acta, 60, 2595-2608.

Cherniak, D.J., Watson, E.B., and Wark, D.A. (2007) Ti diffusion in quartz. Chemical Geology. 236, 65-74.

Cornell, D.H., Brander, L., Zack, T., and Kristoffersen, M. (2013) The Plat Sjambok Anorthosite

and its tonalitic country rocks: Mesoproterozoic pre-tectonic intrusions in the Kaaien Terrane, Namaqua-Natal Province, southern Africa. International Geology Review, 55, 1471-1489.

Deer, W.A., Howie, R.A., and Zussman, J. (1992) An introduction to the rock-forming minerals (Vol. 2). Hong Kong: Longman Scientific & Technical.

Ferry, J.M., and Watson, E.B. (2007) New thermodynamic models and revised calibrations for the Ti-in-zircon and Zr-in-rutile thermometers. Contributions to Mineralogy and Petrology, 154, 429-437.

Frey, M., Desmons, J., and Neubauer, F. (1999) The new metamorphic map of the Alps: introduction. Schweizerische Mineralogische und Petrographische Mitteilungen, 79, 1-4.

Geological Institute, University of Bern, and Federal Office for Water und Geology. (2005) 1:500000. Geological Map of Switzerland. ISBN number: 3-906723-39-9.

Giletti, B.J., and Yund, R.A. (1984) Oxygen Diffusion in Quartz. Journal of Geophysical Research, 89, 4039-4046.

Graeser, S. (1968) Lead isotopes and minor elements in galenas and sulphosalts from Binnatal. Earth and Planetary Science Letters, 4, 384-392.

Harrison, T.M., and Schmitt, A.K. (2007) High sensitivity mapping of Ti distributions in Hadean zircons. Earth and Planetary Science Letters, 261, 9-19.

Hofmann, B.A., and Knill, M.D. (1996) Geochemistry and genesis of the Lengenbach Pb-Zn-As-Tl-Ba-mineralisation, Binn Valley, Switzerland. Mineralium Deposita, 31, 319-339.

Huang, R., and Audétat, A. (2012) The titanium-in-quartz (TitaniQ) thermobarometer: A critical examination and re-calibration. Geochimica et Cosmochimica Acta, 84, 75-89.

Janots, E., Berger, A., Gnos, E., Whitehouse, M., Lewin, E., and Pettke, T. (2012) Constraints on

fluid evolution during metamorphism from U–Th–Pb systematics in Alpine hydrothermal monazite. Chemical Geology, 326-327, 61-71.

Jochum, K.P., and Stoll, B. (2008) Reference materials for elemental and isotopic analysis by LA-(MC)-ICP-MS: successes and outstanding needs. In: Sylvester, P. (ed) Laser Ablation ICP-MS in the Earth Sciences: Current practices and outstanding issues. Mineralogical Society of Canada, 40, 147-168.

Kita, N.T., Huberty, J.M., Kozdon, R., Beard, B.L., and Valley, J.W. (2011) High-precision SIMS oxygen, sulfur and iron stable isotope analyses of geological materials: accuracy, surface topography and crystal orientation. Surface and Interface Analysis, 43, 427-431.

Klemme, S., Prowatke, S., Münker, C., Magee, C.W., Lahaye, Y., Zack, T., Kasemann, S.A., Cabato, E.J.A., and Kaeser, B. (2008) Synthesis and preliminary characterisation of new silicate, phosphate and titanite reference glasses. Geostandards and Geoanalytical Research, 32, 39-54.

Luvizotto, G.L., Zack, T., Meyer, H.P., Ludwig, T., Triebold, S., Kronz, A., Münker, C., Stockli, D.F., Prowatke, S., Klemme, S., Jacob, D.E., and Eynatten, H.v. (2009a) Rutile crystals as potential trace element and isotope mineral standards for microanalysis. Chemical Geology, 261, 346–369.

Luvizotto, G.L., Zack, T., Triebold, S., and von Eynatten, H. (2009b) Rutile occurrence and trace element behavior in medium-grade metasedimentary rocks: examples from Erzgebirge, Germany. Mineralogy and Petrology, 97, 233-249.

Luvizotto, G.L., and Zack, T. (2009) Nb and Zr behavior in rutile during high-grade metamorphism and retrogression: An example from the Ivrea-Verbano Zone. Chemical Geology, 261, 303-317.

Matthews, A. (1994) Oxygen isotope geothermometers for metamorphic rocks. Journal of Metamorphic Geology, 12, 211-219.

Matthews, A., and Schliestedt, M. (1984) Evolution of the blueschist and greenschist facies rocks of Sifnos, Cyclades, Greece. Contributions to Mineralogy and Petrology, 88, 150-163.

Mezger, K., Hanson, G.N., and Bohlen, S.R. (1989) High-precision UPb ages of metamorphic rutile: application to the cooling history of high-grade terranes. Earth and Planetary Science Letters, 96, 106-118.

Milnes, A.G. (1978) Structural zones and continental collision, Central Alps. Tectonophysics, 47, 369-392.

Moore, D.K., Cherniak, D.J., and Watson, E.B. (1998) Oxygen diffusion in rutile from 750 to 1000 8°C and 0.1 to 1000 MPa. American Mineralogist, 83, 700–711.

Mullis, J. (1996) P-T-t path of quartz formation in extensional veins of the Central Alps. Schweizerische Mineralogische und Petrographische Mitteilungen, 76, 159-164.

Mullis, J., Dubessy, J., Poty, B., and O'Neil, J. (1994) Fluid regimes during late stages of a continental collision: Physical, chemical, and stable isotope measurements of fluid inclusions in fissure quartz from a geotraverse through the Central Alps, Switzerland. Geochimica et Cosmochimica Acta, 58, 2239-2267.

Poty, B.P., Stalder, H.A., and Weisbrod, A.M. (1974) Fluid inclusions studies in quartz from fissures of Western and Central Alps. Schweizerische Mineralogische und Petrographische Mitteilungen, 54, 717-752.

Praeger, M., and Crumbach, M. (2004) Aeschynit, Fergusonit und Zirkon vom Wannigletscher (CH). Mineralien Magazin Lapis, 29, 59-64.

Ring, U. (1992) The Alpine geodynamic evolution of Penninic nappes in the eastern Central

Alps: geothermobarometric and kinematic data. Journal of Metamorphic Geology, 10, 33-53.

Rütti, R. (2003) The tectono-metamorphic evolution of the northwestern Simano Nappe (Central Alps, Switzerland), 150 p. Ph.D thesis, Swiss Federal Institute of Technology Zurich.

Rütti, R., Maxelon, M., and Mancktelow, N.S. (2005) Structure and kinematics of the northern Simano Nappe, Central Alps, Switzerland. Eclogae Geologicae Helvetiae, 98, 63–81.

Schmitt, A.K., and Zack, T. (2012) High-sensitivity U–Pb rutile dating by secondary ion massspectrometry (SIMS) with an O2+ primary beam. Chemical Geology, 332-333, 65–73.

Seifert, W., Rhede, D., Thomas, R., Förster, H.J., Lucassen, F., Dulski, P., and Wirth, R. (2011) Distinctive properties of rock-forming blue quartz: inferences from a multi-analytical study of submicron mineral inclusions. Mineralogical Magazine, 75, 2519-2534.

Sharp, Z.D., Masson, H., and Lucchini, R. (2005) Stable isotope geochemistry and formation mechanisms of quartz veins; extreme paleoaltitudes of the central alps in the neogene. American Journal of Science, 305, 187-219.

Taylor, R., Clark, C., and Reddy, S.M. (2012) The effect of grain orientation on secondary ion mass spectrometry (SIMS) analysis of rutile. Chemical Geology, 300-301, 81–87.

Thomas, J.B., Watson, E.B., Spear, F.S., Shemella, P.T., Nayak, S.K., and Lanzirotti, A. (2010) TitaniQ under pressure: the effect of pressure and temperature on the solubility of Ti in quartz. Contributions to Mineralogy and Petrology, 160, 743–759.

Tomkins, H.S., Powell, R., and Ellis, D.J. (2007) The pressure dependence of the zirconium-in-rutile thermometer. Journal of Metamorphic Geology, 25, 703-713.

Trail, D., Bindeman, I.N., Watson, E.B., and Schmitt, A.K. (2009) Experimental calibration of oxygen isotope fractionation between quartz and zircon. Geochimica et Cosmochimica Acta, 73, 7110-7126.

Wark, D.A., and Watson, E.B. (2006) TitaniQ: a titanium-in-quartz geothermometer. Contributions to Mineralogy and Petrology, 152, 743–754.

Watson, E.B., Wark, D.A., and Thomas, J.B. (2006) Crystallization thermometers for zircon and rutile. Contributions to Mineralogy and Petrology, 151, 413-433.

Zack, T., Moraes, R., and Kronz, A. (2004) Temperature dependence of Zr in rutile: empirical calibration of a rutile thermometer. Contributions to Mineralogy and Petrology, 148, 471–488.

Zack, T., Stockli, D.F., Luvizotto, G.L., Barth, M.G., Belousova, E., Wolfe, M.R., and Hinton, R.W. (2011) In-situ U-Pb rutile dating by LA-ICP-MS: 208Pb correction and prospects for geological applications. Contributions to Mineralogy and Petrology, 162, 515-530.

Zhang, R.Y., Zhai, S.M., Fei, Y.W., and Liou, J.G. (2003) Titanium solubility in coexisting garnet and clinopyroxene at very high pressure: the significant of exsolved rutile in garnet. Earth and Planetary Science Letters, 216, 591-601.

Zheng, Y.F. (1991) Calculation of oxygen isotope fractionation in metal oxides. Geochimica et Cosmochimica Acta, 55, 2299-2307.

FIGURE CAPTIONS

Figure 1. Samples 1-6 plotted on Digital Elevation Model (DEM) of Central Swiss Alps. Inset is Switzerland showing DEM region. Thin white lines are the Switzerland border. Thick, dashed lines are metamorphic isotherms (Bousquet et al. 2012). Thin, black lines represent major Swiss

rock units and thinnest black lines show major lineaments (1:500,000 map of the Geological Institute, University of Bern, and Federal Office for Water and Geology). HN = Helvetic Nappes; BS = Bündnerschiefer; GM = Gotthard Massif; LE = Lepontine Dome.

Figure 2. Sample 1 mounted fragment. Two rutile needles exposed on the mounted surface are boxed and shown in (**2b**). (**a**) CL image. Light and dark regions of the quartz illustrate complex oscillatory and sector zoning, suggesting multiple generations of quartz growth. (**b**) Enlarged boxed region in (**2a**) showing rutile. Transmitted light image detail shows the location of SIMS and LA-ICP-MS analysis spots and corresponding compositions.

Figure 3. CL image of Sample 4 mounted fragment. Rutiles are circled in white and shown in more detail in (**3b**) and (**3c**). Light and dark regions in host quartz show generations of growth. (**3b**) and (**3c**) are transmitted light images of individual rutiles. SIMS and LA-ICP-MS analyses and values are noted on the image.

Figure 4. (**a**) CL image of Sample 6 fragment. (**b**) BSE image of rutile needle 1. (**c**) BSE image of rutile needle 2 showing zoning. Trace element causing zoning was not determined. SIMS and LA-ICP-MS analyses and compositions are noted on the image.

Figure 5. SIMS vs. bulk laser fluorination analysis of ^{18}O and ^{16}O in rutile standards (Luvizotto et al. (2009a) and Schmitt and Zack (2012) for description of natural and synthetic rutiles). SIMS instrumental mass fractionation is corrected for rutile standard R10b ($\delta^{18}O$ = 6.60 ‰). The deviation of the SIMS values from the bulk values is 0.18 ‰ (without Sy) and 0.49 ‰ (with Sy) averaging multiple spots on randomly oriented fragments. Errors plotted are 1σ for clarity.

Figure 6. Time-series of oxygen isotope analyses of glass and R10b rutile for different SIMS analytical conditions (see text). (**a**) 5 kV Cs^+ primary beam; (**b**) 10 kV Cs^+ beam without (gray) and with (black) correction for secondary ion yield (where instrumental mass fractionation is

fitted linearly against the secondary ion intensity normalized to the primary beam ion intensity). Errors plotted are 1σ for clarity.

Figure 7. Tera-Wasserburg concordia diagram for Samples 1-6 without common Pb correction. Linear regression yields a concordia intercept age of 15.1 ± 1.7 Ma (2σ; n = 21). Common Pb (y-axis) intercept value at $^{207}Pb/^{206}Pb = 0.833 \pm 0.006$ is within uncertainty of galena in regional hydrothermal veins.

Figure 8. Logarithmic plots of Zr concentration in rutile and Ti concentration in quartz versus the square-root of quartz-rutile oxygen isotope fractionation (proportional to 1/T, with T indicated by the top axis values using the calibration of Matthews, 1994). Experimental calibrations of Tomkins et al. (2007) and Zack et al. (2004) are shown for comparison in (**a**), and those of Thomas et al. (2010) and Huang and Audétat (2012) in (**b**). Errors plotted are 1σ for clarity.

Figure 9. Graphical summaries of all trace element (Tomkins et al. 2007; Huang and Audétat 2012) and oxygen isotope thermometry (Matthews 1994) data from Samples 1-6 in P vs. T space. Samples 1-6 correspond to panels (**a**) – (**f**), respectively. Average values per rutile needle per sample are plotted. If two needles were analyzed per sample, needle 1 is represented by the thicker lines and 2 by the thinner lines. Error bars for oxygen isotope thermometry are shown; nominal analytical errors for Zr-in-rutile and Ti-in-quartz thermobarometers are within the thickness of the plotted lines. Errors plotted are 1σ. Pressures ranging from 0-8 kbar represent absolute minimum and maximum formation conditions for the sampled veins based on existing barometry for Alpine fissure mineralization and reasonable geologic constraints.

APPENDIX

Appendix 1. U-Th-Pb rutile analysis results.

Appendix 2. Oxygen isotope and Ti-in-quartz results determined via SIMS. Temperature and errors are graphically shown in Figure 9.

Appendix 3. Zr-in-rutile and other trace elements concentrations determined via the LA-ICP-MS system (213 nm NWR New Wave laser coupled to an Agilent 7500a) at the University of Gothenburg, Sweden.

Appendix 4. Complete list of Zr-in-rutile, Ti-in-quartz, and oxygen isotope thermometry data that is plotted in Figure 9.

TABLES

Table 1. SIMS oxygen isotope data for newly developed rutile standards. Results from several round-robin sessions of three analytical and correction protocols are shown.

Table 2. Summary of oxygen isotope fractionation, Zr-in-rutile, and Ti-in-quartz data. Data is represented as average value of analysis type per rutile needle per sample.

qtz = quartz

rut = rutile

1 s.d. [‰] = one standard deviation

a = one Ti-in-quartz data point that deviated greater than one standard deviation from the mean excluded from rutile needle average

b = calculated from Huang and Audétat (2012)

Figure 1.

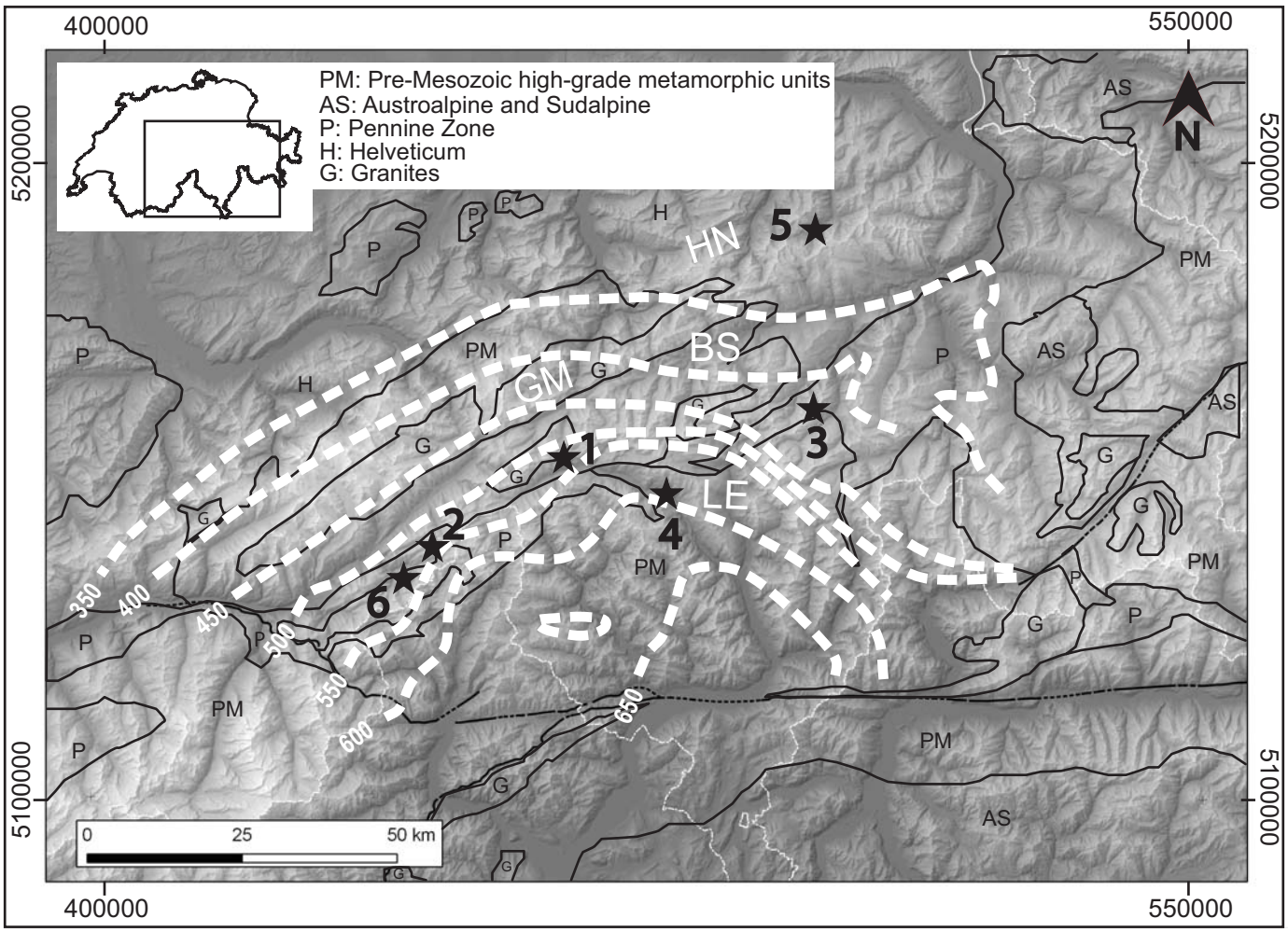
400000
550000
5200000
5100000
PM: Pre-Mesozoic high-grade metamorphic units
AS: Austroalpine and Sudalpine
P: Pennine Zone
H: Helveticum
G: Granites
N
HN
BS
GM
LE
1
2
3
4
5
6
350
400
450
500
550
600
650
0
25
50 km

Figure 2.

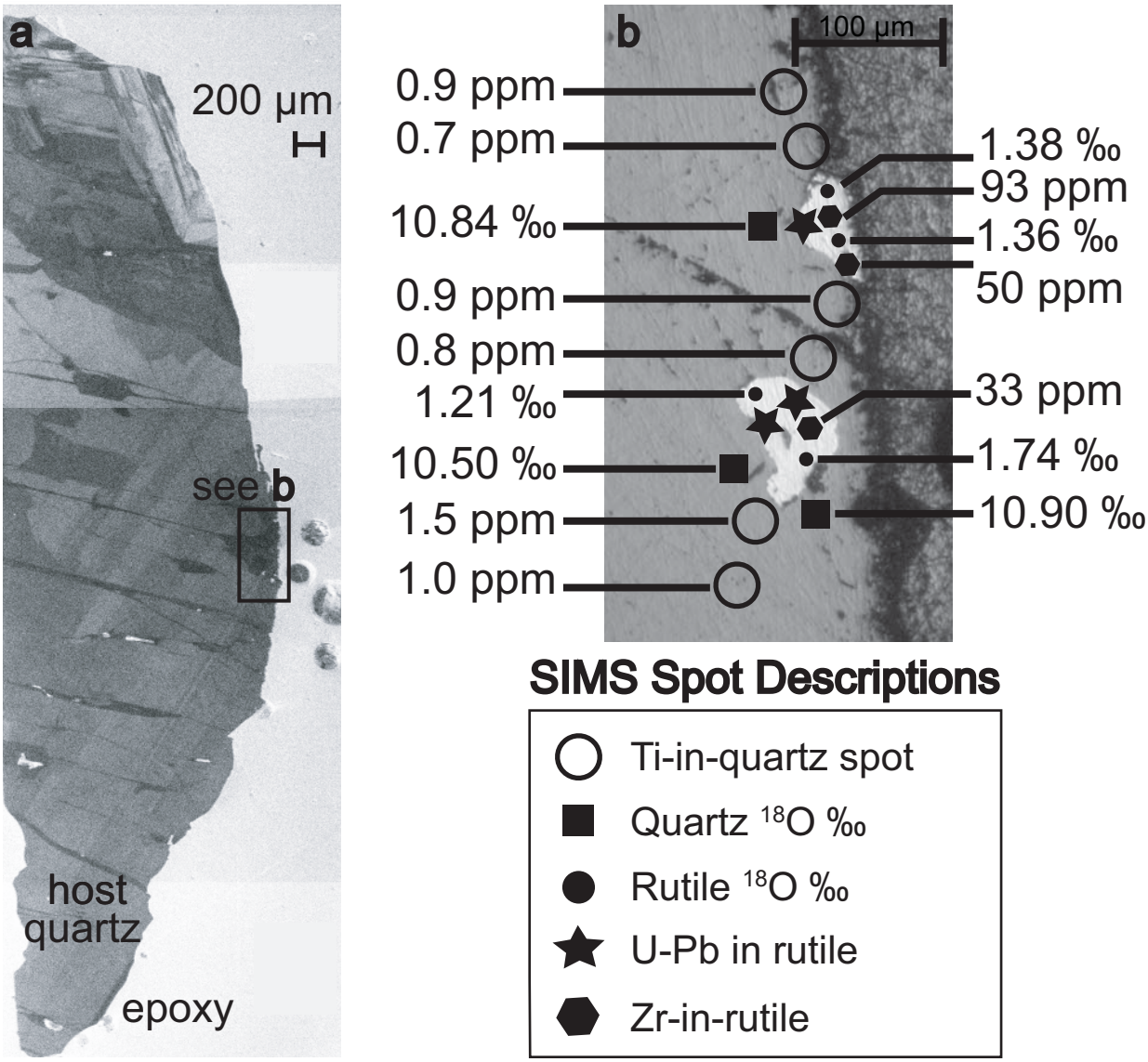
a
200 µm
see b
host quartz
epoxy
b
100 µm
0.9 ppm
0.7 ppm
10.84 ‰
0.9 ppm
0.8 ppm
1.21 ‰
10.50 ‰
1.5 ppm
1.0 ppm
1.38 ‰
93 ppm
1.36 ‰
50 ppm
33 ppm
1.74 ‰
10.90 ‰
SIMS Spot Descriptions
Ti-in-quartz spot
Quartz 18O ‰
Rutile 18O ‰
U-Pb in rutile
Zr-in-rutile

Figure 3.

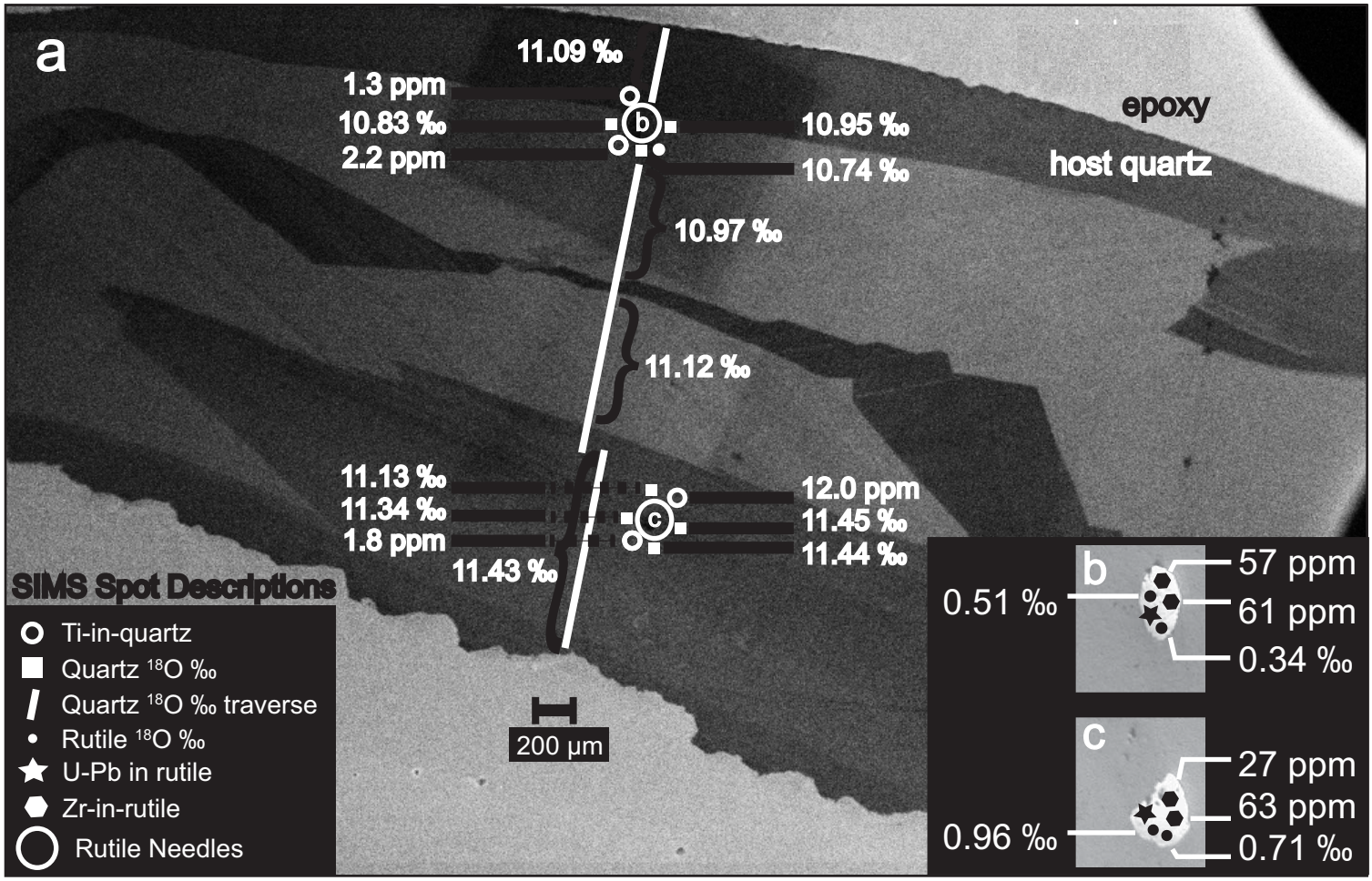
a
11.09 ‰
1.3 ppm
10.83 ‰
2.2 ppm
b
10.95 ‰
10.74 ‰
epoxy
host quartz
10.97 ‰
11.12 ‰
11.13 ‰
11.34 ‰
1.8 ppm
11.43 ‰
c
12.0 ppm
11.45 ‰
11.44 ‰
SIMS Spot Descriptions
Ti-in-quartz
Quartz 18O ‰
Quartz 18O ‰ traverse
Rutile 18O ‰
U-Pb in rutile
Zr-in-rutile
Rutile Needles
200 µm
0.51 ‰
b
57 ppm
61 ppm
0.34 ‰
c
27 ppm
63 ppm
0.96 ‰
0.71 ‰

Figure 4.

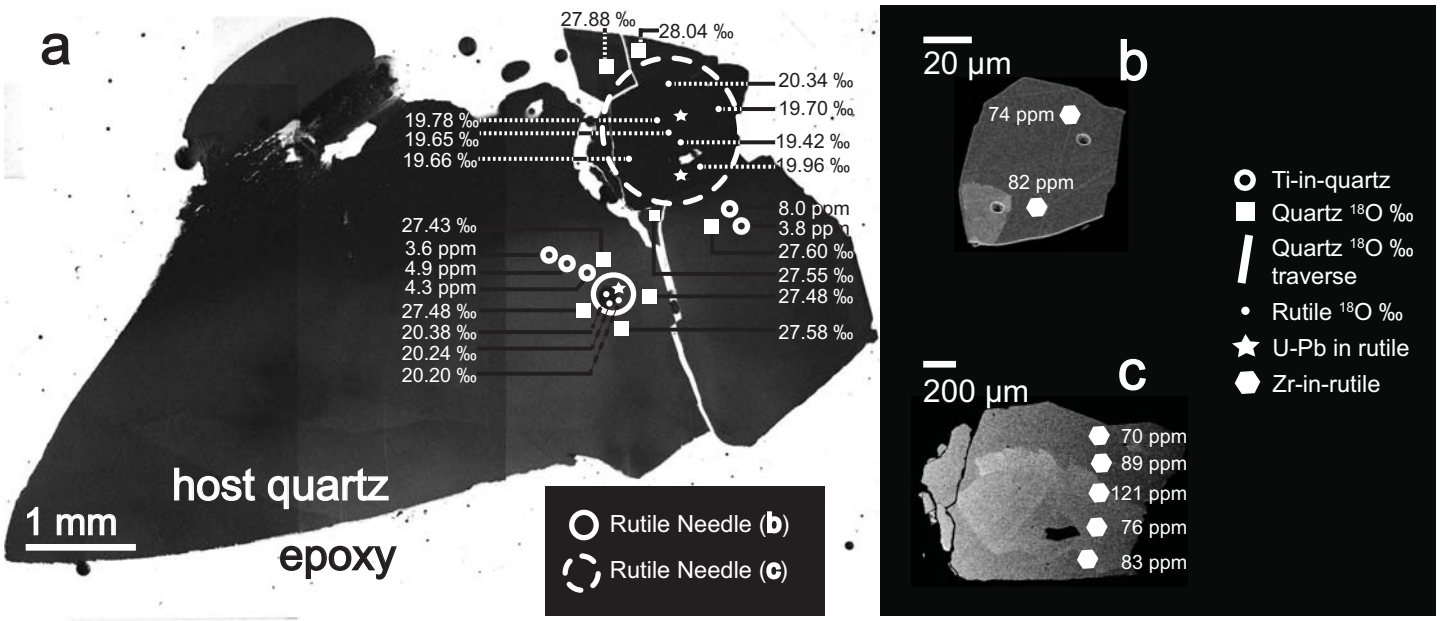
a
27.88 ‰
28.04 ‰
20.34 ‰
19.70 ‰
19.78 ‰
19.65 ‰
19.66 ‰
19.42 ‰
19.96 ‰
8.0 ppm
27.43 ‰
3.6 ppm
4.9 ppm
4.3 ppm
27.60 ‰
27.55 ‰
27.48 ‰
27.48 ‰
20.38 ‰
20.24 ‰
20.20 ‰
27.58 ‰
host quartz
1 mm
epoxy
Rutile Needle (b)
Rutile Needle (c)
20 µm
b
74 ppm
82 ppm
Ti-in-quartz
Quartz 18O ‰
Quartz 18O ‰ traverse
Rutile 18O ‰
U-Pb in rutile
Zr-in-rutile
200 µm
c
70 ppm
89 ppm
121 ppm
76 ppm
83 ppm

Figure 5.

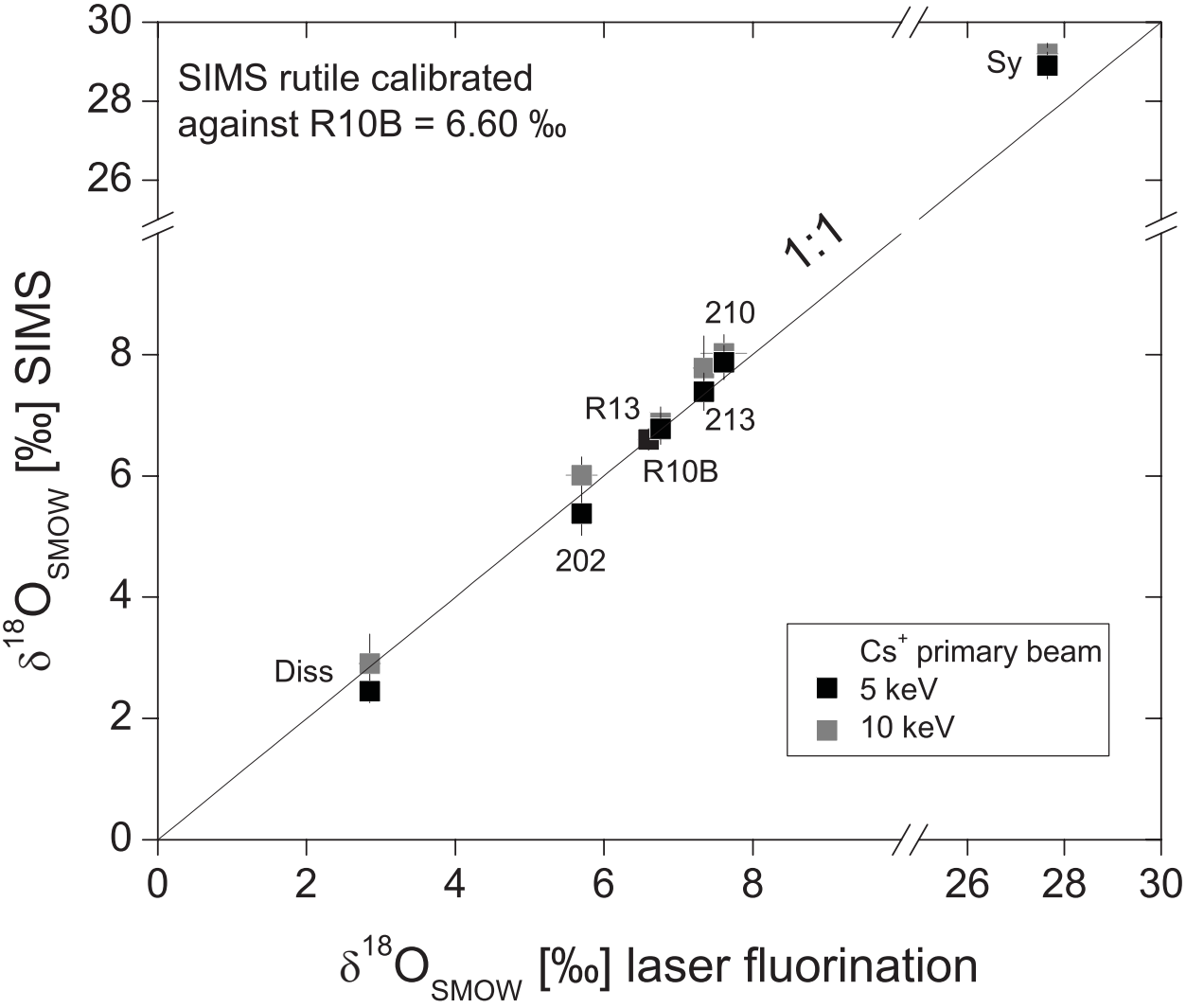
SIMS rutile calibrated
against R10B = 6.60 ‰
1:1
Sy
210
213
R13
R10B
202
Diss
Cs+ primary beam
5 keV
10 keV
δ18OSMOW [‰] SIMS
δ18OSMOW [‰] laser fluorination
0
2
4
6
8
26
28
30

Figure 6.

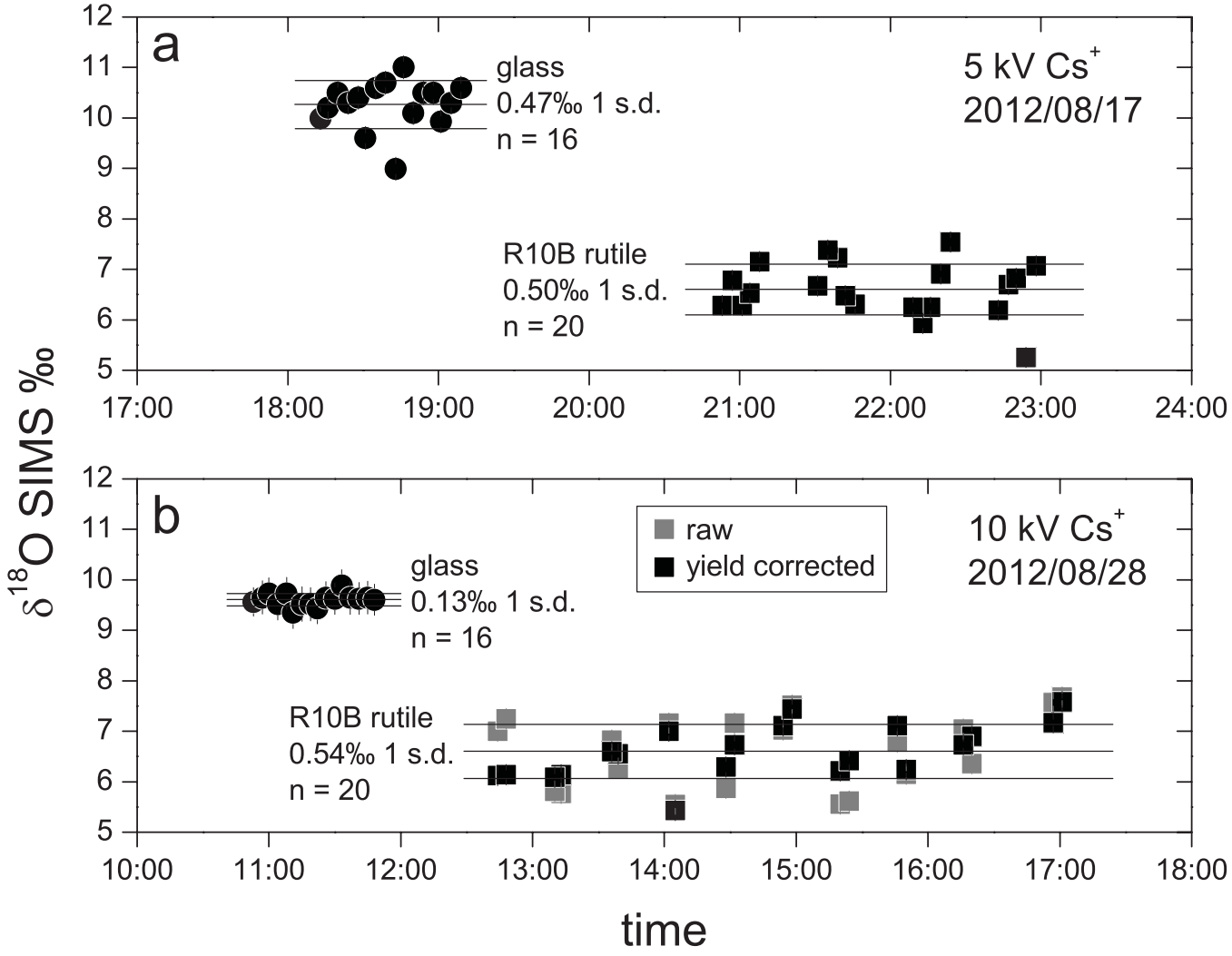
a
glass
0.47‰ 1 s.d.
n = 16
5 kV Cs+
2012/08/17
R10B rutile
0.50‰ 1 s.d.
n = 20
b
raw
yield corrected
glass
0.13‰ 1 s.d.
n = 16
10 kV Cs+
2012/08/28
R10B rutile
0.54‰ 1 s.d.
n = 20
δ18O SIMS ‰
time

Figure 7.

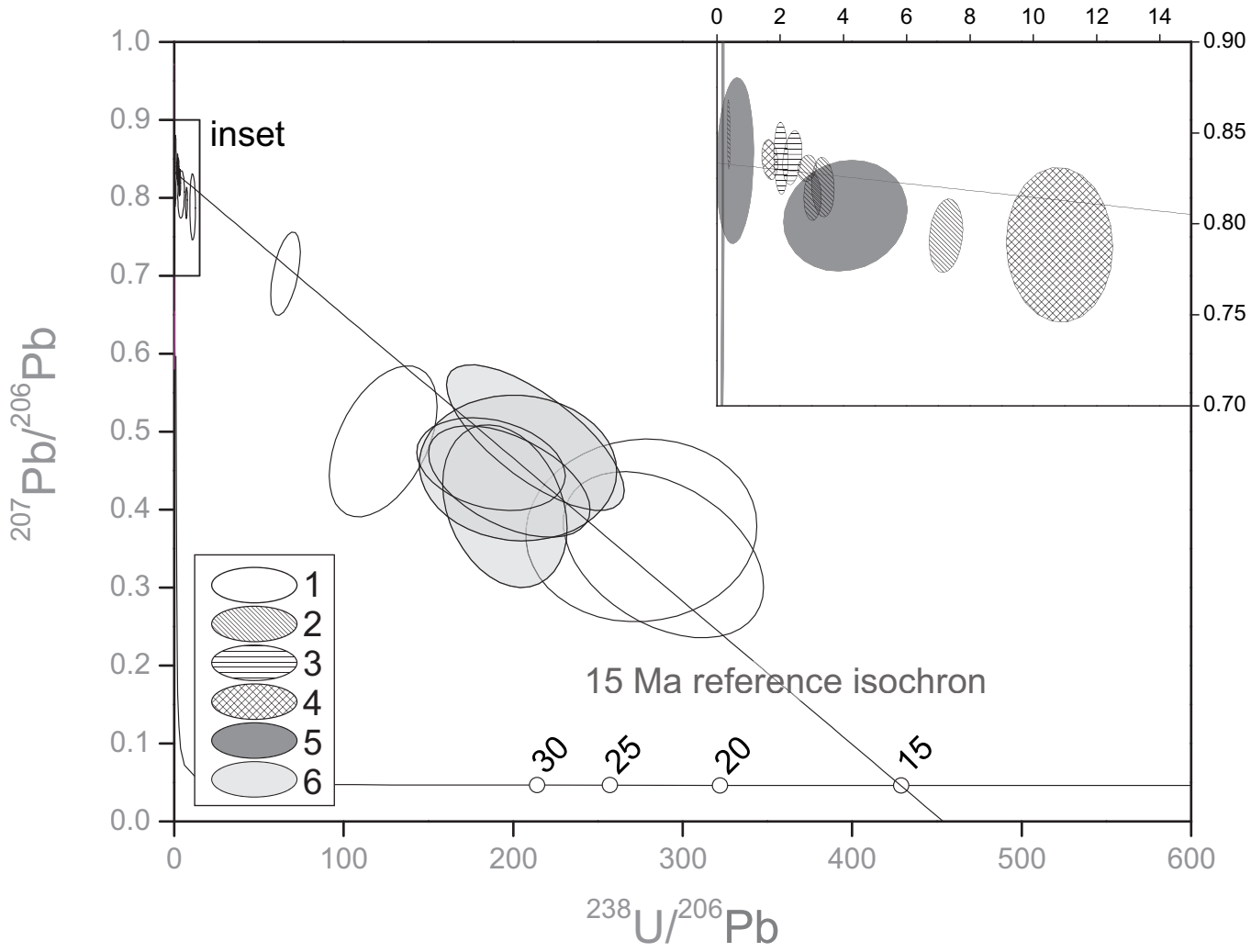
inset
15 Ma reference isochron
30
25
20
15
1
2
3
4
5
6
$^{207}Pb/^{206}Pb$
$^{238}U/^{206}Pb$

Figure 8.

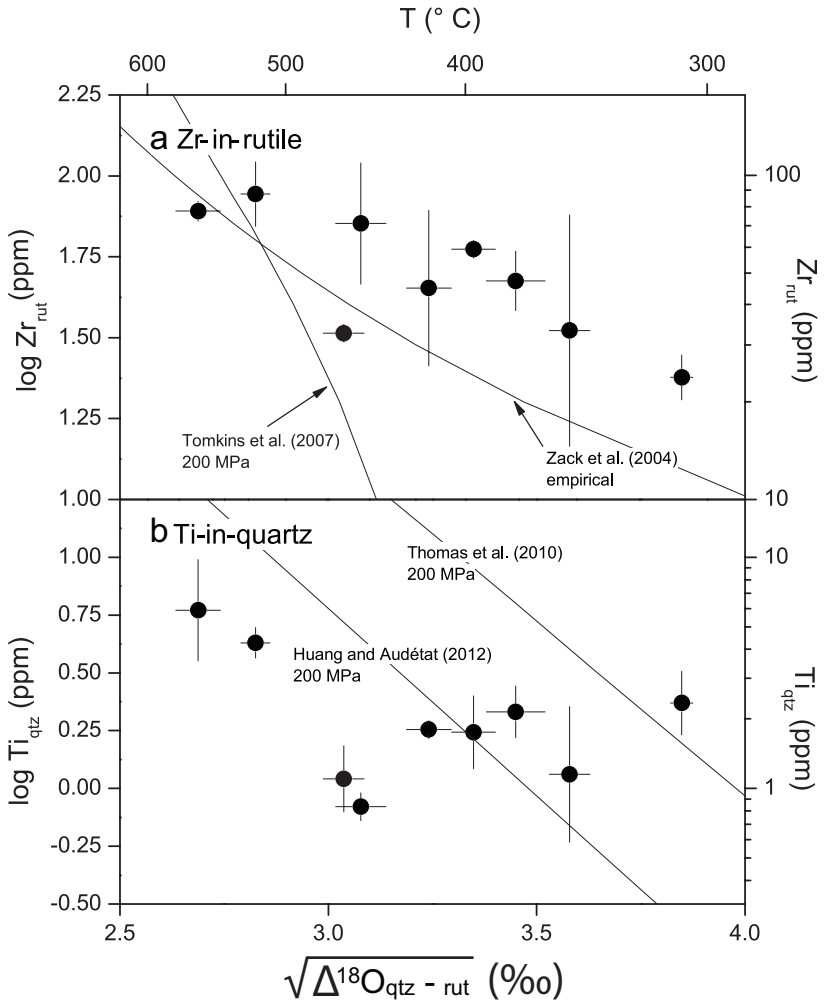
T (° C)
600
500
400
300
a Zr-in-rutile
log Zr rut (ppm)
Zr rut (ppm)
Tomkins et al. (2007)
200 MPa
Zack et al. (2004)
empirical
b Ti-in-quartz
Thomas et al. (2010)
200 MPa
Huang and Audétat (2012)
200 MPa
log Ti qtz (ppm)
Ti qtz (ppm)
√Δ18Oqtz - rut (‰)

Figure 9.

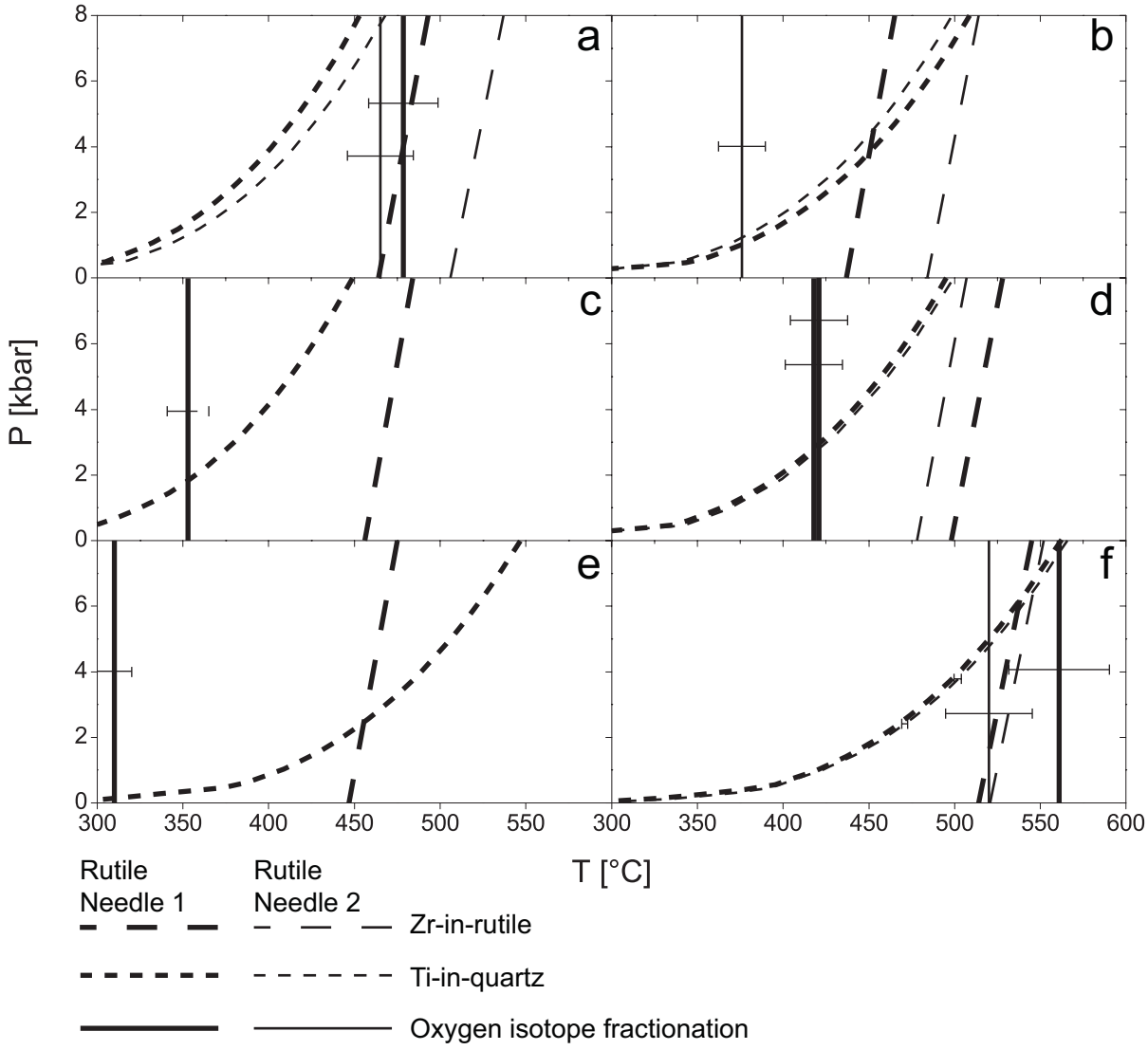
a
b
c
d
e
f
P [kbar]
T [°C]
Rutile Needle 1
Rutile Needle 2
Zr-in-rutile
Ti-in-quartz
Oxygen isotope fractionation

Table 1.

	Laser fluorination[a]			**SIMS 10kV Cs^+**			**SIMS 10kV Cs^+ (yield corrected)**			**SIMS 5kV Cs**
average IMF				0.9946			0.9946			0.9978
standard deviation glass [‰]				0.13			0.13			0.39
Rutile	**$\delta^{18}O$[‰]**	**n**	**2 s.e.**	**[‰]**	**n**	**2 s.e.**	**$\delta^{18}O$[‰]**	**n**	**2 s.e.**	**$\delta^{18}O$[‰]**
R10B[b]	6.60	3	0.034	6.60	60	0.20	6.60	60	0.17	6.60
R13	6.76	4	0.025	6.87	15	0.26	6.87	15	0.27	6.78
210	7.61	4	0.157	8.02	10	0.31	8.02	10	0.31	7.87
202	5.70	3	0.121	6.00	10	0.30	6.01	10	0.30	5.38
Sy	27.7	2	0.115	29.7	10	0.52	29.2	10	0.16	28.9
Diss	2.85	1	0.100	3.06	10	0.41	2.91	10	0.48	2.45
213	7.34	2	0.100	7.24	10	0.19	7.78	10	0.53	7.39

IMF = instrumental mass fractionation.

n = number of replicates (individual fragments for laser fluorination; spots for SIMS).

s.e. = standard error of the mean.

[a]Laser fluorination against UOG and Gore Mountain garnet (correction +0.07‰; n = 4).

[b]used as standard for SIMS IMF correction.

+

n	2 s.e.
79	0.13
14	0.26
11	0.28
11	0.36
12	0.34
5	0.19
11	0.31

Table 2.

Sample #	Needle #	# qtz spots averaged	# rut spots averaged	$\Delta^{18}O_{qtz\text{-}rut}$ [‰]	1 s.d. [‰]	Temperature (°C) $\Delta^{18}O_{qtz\text{-}rut}$ [a]	$\Delta^{18}O_{qtz\text{-}rut}$ T error
1	1	2	3	9.22	0.30	465	40
	2	1	2	9.47	0.37	455	38
2	1		2				
	2	4	1	11.90	0.5	376	27
3	1	4	2	12.81	0.3	353	24
4	1	3	2	10.42	0.4	421	33
	2	4	2	10.51	0.3	418	33
5	1	6	6	14.81	0.2	310	20
6	1	4	3	7.22	0.29	561	58
	2	4	7	7.98	0.20	520	50
		error per qtz analysis [‰]	error per rutile analysis [‰]				
		0.15	0.48				

qtz = quartz.

rut = rutile.

1 s.d. [‰] = one standard deviation.

[a] = calculated from Matthews (1994).

[b] = one Ti-in-quartz data point that deviated greater than one standard deviation from the mean excluded from rutile needle

√(Δ^{18}O$_{qtz-rut}$ [‰])	# Zr spots averaged	Zr ppm	Zr 1 s.d. (ppm)	# Ti spots averaged	Ti ppm	absolute error in ppm
3.0	1	32.6	1.6	3	1.10	0.07
3.1	2	71.3	30.7	3	0.83	0.07
0.0	2	19.0	1.4	2	1.80	0.10
3.4	2	47.3	10.0	2	2.14	0.16
3.6	2	33.3	27.4	3	0.90	0.19
3.2	2	59.3	2.8	2	1.75	0.10
3.2	2	45.0	24.9	1	1.80[b]	0.12
3.8	6	23.8	3.8	5	2.34[b]	0.17
2.7	2	77.9	5.5	2	5.90	0.27
2.8	5	87.9	20.1	3	4.27	0.22

average.